Strain-induced Anisotropic Terahertz Emission From a Fe(211)/Pt(110) Bilayer

C.Q. Liu,[1,†] W.-T. Lu,[2,†] Z.X. Wei,[3,†] Y.F. Miao,[2] P. Wang,[1] H. Xia,[1] Y.P. Liu,[3] F.L. Zeng,[1]
J.R. Zhang,[1] C. Zhou,[1] H.B. Zhao,[4] Y.Z. Wu,[1,5,*] Z. Yuan,[2,‡] and J. Qi[3,§]

[1] *Department of Physics, State Key Laboratory of Surface Physics, Fudan University, Shanghai 200433, China*
[2] *The Center for Advanced Quantum Studies and Department of Physics, Beijing Normal University, Beijing 100875, China*
[3] *State Key Laboratory of Electronic Thin Films and Integrated Devices, University of Electronic Science and Technology of China, Chengdu 610054, China*
[4] *Shanghai Ultra-precision Optical Manufacturing Engineering Research Center, and Key Laboratory of Micro and Nano Photonic Structures (Ministry of Education), Department of Optical Science and Engineering, Fudan University, Shanghai 200433, China*
[5] *Shanghai Research Center for Quantum Sciences, Shanghai 201315, China*

(Received 2 February 2021; accepted 25 March 2021; published 13 April 2021)

Terahertz (THz) emission from a Fe(211)/Pt(110) bilayer grown on MgO(110) is systematically investigated. The intensity of the emitted THz wave strongly depends on the magnetization (**M**) orientation, and the measured THz field is 11% larger for **M**||Pt[$1\bar{1}0$] than for **M**||Pt[001]. Using first-principles calculations combined with the superdiffusive spin-transport model, we reveal that the lattice distortion induced by epitaxial strain causes anisotropic behavior of the electronic conductance and spin Hall conductivity, which eventually lead to the aforementioned experimental observations. Our studies thus provide a route to modify THz emission utilizing the intrinsic crystal-structure degree of freedom.

DOI: 10.1103/PhysRevApplied.15.044022

I. INTRODUCTION

Terahertz (THz) electromagnetic waves, which lie in the gap between microwave and infrared radiation in spectroscopy [1–3], offer great prospects for imaging, sensing, and security applications. The ferromagnetic (FM) and heavy metal (HM) heterostructure has recently attracted extensive attention since it was demonstrated to be an efficient and broadband THz source [4–11]. In this type of heterostructure, photoexcitation of the FM layer with femtosecond (fs) laser pulses first generates nonequilibrium carriers that are transmitted into the neighboring HM layer, consequently leading to an ultrafast spin current. At the same time, due to the inverse spin Hall effect (ISHE), such a spin current can be converted into a transient charge current, which finally generates a short terahertz pulse with its polarization perpendicular to the magnetization in the FM layer [4]. In addition to ISHEs, other spin-to-charge conversion (SCC) mechanisms, such as the inverse Rashba-Edelstein effect (IREE), have also been shown to generate THz emission [12–14]. Therefore, the FM-HM heterostructure is often referred to as the spintronic THz emitter (STE).To date, research on STEs has mainly focused on controlling two properties of the THz wave: intensity and polarization. For the former, high THz emission efficiency has been found in newly designed STE structures, such as FM-HM multilayer stacks [6,10] and Pt/(Co, Fe)B/W sandwiches, which utilize the opposite spin Hall angles of Pt and W [9]. For the latter, a linearly polarized broadband THz wave from a STE can be conveniently manipulated by rotating the magnetic field, while the intensity of the emitted THz wave is nearly unchanged [6,15]. In fact, manipulation of these two properties as well as the bandwidth can be simultaneously realized in patterned stripe structures [6,16,17].

In most of the studies in the literature, STEs are made of polycrystalline films [7,18–21], and hence some characteristics uniquely associated with single-crystal films do not arise, e.g., the crystal structure dependence of spin-orbit-coupling- (SOC) induced effects. In particular, (1) nonmagnetic (NM) materials with the hexagonal close-packed (hcp) structure [22] and antiferromagnets, such as PtMn [23], exhibit a strong anisotropy in the spin Hall effect (SHE); and (2) the anisotropic magnetoresistance and Gilbert damping coefficient in single-crystal CoFe films show a strong dependence on the crystalline orientation of the magnetization and/or the electrical current [24,25]. Therefore, the ISHE in systems with a lower symmetry is supposed to have a strong anisotropy. As a

---

[*] wuyizheng@fudan.edu.cn
[†] These authors contributed equally.
[‡] zyuan@bnu.edu.cn
[§] jbqi@uestc.edu.cn

result, the THz emission may show its dependence on the magnetization orientation. Therefore, a key question is whether manipulation of the emitted THz wave could be achieved by tuning the intrinsic crystal symmetry.

In this work, we investigate the THz emission from Fe(211)/Pt(110) single-crystal film grown on MgO(110) substrates and demonstrate that the intensity of the emitted THz wave strongly depends on the magnetization orientation **M**. Specifically, the measured THz electric field for **M**||Pt[$1\bar{1}0$] is 11.0% larger than that for **M**||Pt[001]. Our experimental data and first-principles calculations indicate that both the spin-current generation and its subsequent injection into the Pt layer are independent of the **M** orientation, but the SCC efficiency in the Pt layer as well as the associated THz wave radiation can be greatly affected by the **M** orientation due to the anisotropic SHE and longitudinal conductance in the Fe/Pt bilayer, which gives rise to the anisotropic THz emission. Our theoretical results clarify that this anisotropic THz emission can be mainly attributed to lattice distortion in the film induced by epitaxial strain. Therefore, our findings not only demonstrate the intrinsic crystal-structure degree of freedom to manipulate the THz emission, but also show the possibility of modifying the SOC-related properties in the films by applying the strain.

II. EXPERIMENTAL METHODS

The Fe(2 nm)/Pt(2 nm)/MgO(110) films are prepared by molecular beam epitaxy in an ultrahigh vacuum (UHV) system with a base pressure of 2×10^{-10} Torr [26]. The MgO(110) single-crystal substrate is first annealed at 700 °C for 45 min to form an ordered surface, which can be confirmed by sharp reflection high-energy electron diffraction (RHEED) patterns. The Pt film is then grown using a pulse laser deposition (PLD) technique with a 248-nm KrF excimer laser. The first 1-nm Pt film is deposited at 550 °C, and the remaining Pt layer is grown at room temperature. The Fe film is subsequently grown on top of the Pt layer at room temperature via thermal evaporation. The sharp RHEED patterns in Figs. 1(a) and 1(b) indicate that both the Pt and Fe layers are single crystals. The samples are finally capped with a 6-nm Al_2O_3 protection layer before being removed from the growth chamber. The film thickness is then determined by the deposition rate (approximately 1.0–2.0 Å/min), which is measured using a calibrated quartz thickness monitor.

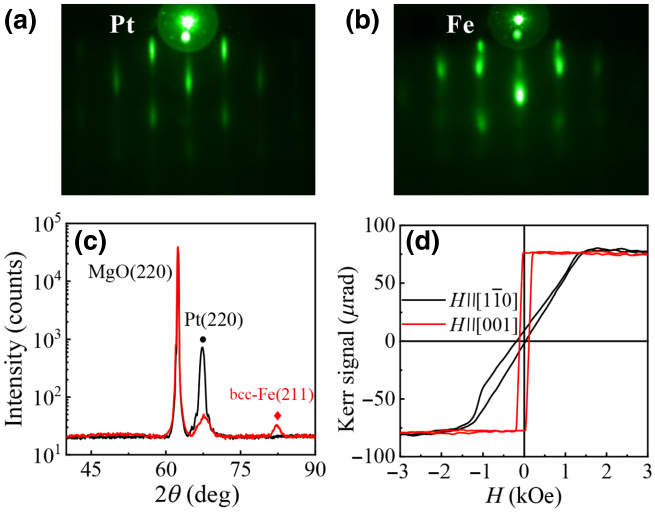

FIG. 1. Typical RHEED patterns of (a) 2-nm Pt and (b) 2-nm Fe grown on MgO(110). The electron beam is along MgO[001] direction. (c) XRD curves of Pt(10 nm)/MgO(110) (black line) and Fe(10 nm)/Pt(2 nm)/MgO(110) (red line). (d) Kerr hysteresis loops of Fe(2 nm)/Pt(2 nm)/MgO(110) with a magnetic field along the Pt[$1\bar{1}0$] and Pt[001] directions.

Figure 1(c) shows the XRD measurements on a Pt(10 nm) layer and a Fe(10 nm)/Pt(2 nm) bilayer. Only fcc-Pt(220) and bcc-Fe(211) peaks can be observed, in addition to the diffraction peaks from the MgO substrate. From the RHEED and XRD measurements, the crystal orientations in every layer can be determined as Fe[$\bar{1}11$](211)||Pt [$1\bar{1}0$](110)||MgO[$1\bar{1}0$](110) [27,28]. However, due to the large lattice mismatch between Fe, Pt, and MgO, there are significant strains acting on both the Fe and Pt layers. After quantitatively analyzing the line profiles of the RHEED patterns from a 2-nm-thick Pt film with the grazing incident electron along the MgO[001] and [$1\bar{1}0$] directions, we determine that the Pt lattice expanded by 2.5% along Pt[001] and shrank by 1.5% along Pt [$1\bar{1}0$] [29]. Based on the structure of the Fe film of Fe(2 nm)/Pt(2 nm)/MgO(110) from the RHEED patterns, we further determine that the Fe lattice expanded 1.7% along Fe[$\bar{1}11$] and shrank 2.4% along Fe[$01\bar{1}$] [29]. Therefore, the in-plane strain imposed in both Fe and Pt films can significantly influence the magnetic properties of the system. Figure 1(d) shows the magnetic hysteresis loops using the longitudinal magneto-optic Kerr effect for the field along the Pt[001] and Pt [$1\bar{1}0$] directions [39,40], respectively. There is clearly an in-plane uniaxial magnetic anisotropy with an easy axis along the Pt[001] direction [29].

In the time-domain THz spectroscopy measurements, a Ti:sapphire oscillator is used with a pulse duration of approximately 35 fs, a central wavelength of 800 nm, and a repetition rate of 80 MHz. The sample is kept inside a pair of permanent magnets with a tunable field strength by varying the separation of the magnets [6,12]. The laser beam is always linearly polarized and normally incident from the substrate side of the sample. The spot size of the laser beam is approximately 150 μm on the samples, and the typical excitation fluence is approximately 14 μJ/cm^2. The THz signals are detected using the electro-optic sampling technique, where the probe pulses from the same laser copropagate with the THz wave through a 0.5-mm-thick ZnTe (110) crystal. All of the experiments are performed at room temperature in a dry-air environment with a humidity less than 4%.

The time-resolved magneto-optical Kerr effect (TR-MOKE) measurement is performed in a longitudinal geometry with a pump laser wavelength of 400 nm and a probe laser wavelength of 800 nm. Detailed information on the TR-MOKE setup can be found in Refs. [41,42]. The laser fluence in the TR-MOKE measurement is fixed at 0.35 mJ/cm^2.

III. EXPERIMENTAL RESULTS

Figure 2(a) is a schematic of the STE made of the Fe(211)/Pt(110) bilayer. Under the excitation of the fs laser pulses, a nonequilibrium spin-polarized current is generated in the Fe film and subsequently superdiffuses into the adjacent Pt film [43], where the injected spin current from the Fe layer into the Pt layer will be converted to an ultrafast charge current via ISHE and then generate a picosecond pulse as a source of THz waves [4,5,7]. Figure 2(b) shows the typical measured THz signals $E_{\mathrm{THz}}(t)$ for different sample orientations. The applied magnetic field is fixed along the x axis, and the THz polarizer is set along the y axis. This configuration means that only the y component of the emitted THz wave can be detected. Note that the applied field is approximately 2.1 kOe, which is well above the saturation field of the hysteresis loop along the hard axis in Fig. 1(d). It is thus clear that the signals in Fig. 2(b) behave nearly the same in the time domain, except that their electric fields vary with the sample orientation. Specifically, the THz field can reach a maximum at a sample orientation angle θ of 90°, i.e., H||Pt$[1\bar{1}0]$. The related anisotropic ratio of the field strength can reach up to 11.0%, which is defined as $[\Delta V(90^{\circ}) - \Delta V(0^{\circ})]/\Delta V(0^{\circ})$, where ΔV denotes the peak-to-peak THz signal. Figure 2(c) presents the Fourier-transformed (FT) spectra in the frequency domain, which show the same θ-dependent behavior as that of the time-domain signals $E_{\mathrm{THz}}(t)$ in Fig. 2(b).

Our experiments are the first to discover this θ-dependent THz emission in STEs. To further discuss this unusual phenomenon, we measure ΔV as a function of θ under three different magnetic fields, as shown in Fig. 3(a). For $H = 2.1$ kOe, there are two obvious peaks at $\theta = 90^{\circ}$ and 270°. For $H = 0.7$ kOe, the THz signals approximately 90° and 270° show obvious valley shapes. For $H = 1.3$ kOe, the THz signals still show peaks at $\theta = 90^{\circ}$ and 270°; however, they exhibit both features from those at fields of 2.1 kOe and 0.7 kOe. In fact, the valleylike shapes with large linewidths for $H = 0.7$ and 1.3 kOe can be attributed to the effect of magnetization tilting. If the magnetic field applied along the hard axis (Pt $<1\bar{1}0>$) is not sufficiently strong, then the magnetization can tilt away

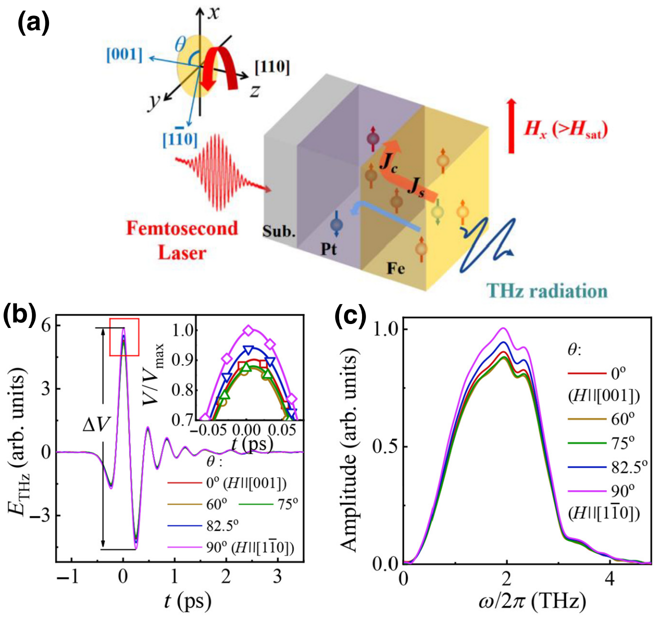

FIG. 2. (a) Schematic of THz emission from the Fe/Pt heterostructure. THz emission along various crystal axes is obtained by rotating the sample with a fixed external magnetic field H_x. (b) Typical time-domain THz signals with different sample azimuth angles. The inset emphasizes the difference in the signals at the peaks. (c) The THz signals in the frequency domain corresponding to the time-domain signals in (b).

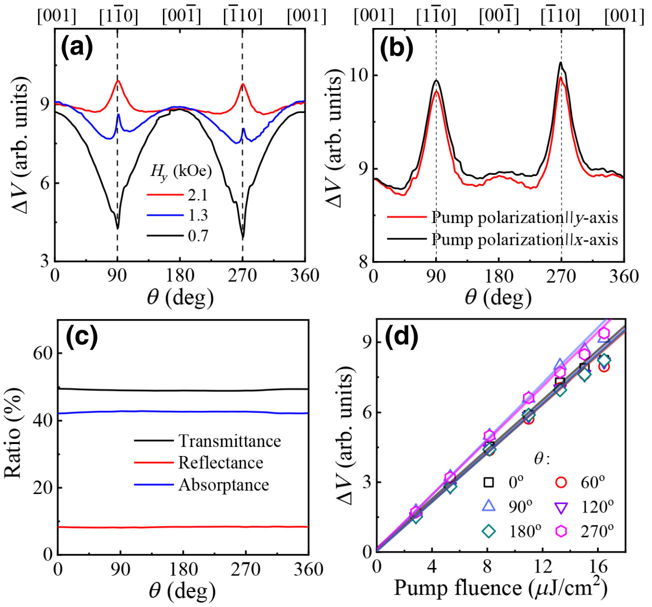

FIG. 3. (a) Peak-to-peak amplitude ΔV of THz emission from a Fe(2 nm)/Pt(2 nm)/MgO(110) sample as a function of the sample azimuth angle θ under external magnetic fields of 0.7, 1.3, and 2.1 kOe. (b) ΔV as a function of θ for the pump polarization along the x axis and y axis. (c) θ dependence of the transmittance, reflectance, and absorptance. (d) ΔV as a function of pump fluence for several θ values.

from the magnetic field (x axis). As a result, the polarization of the emitted THz wave will deviate from the y axis accordingly, thus reducing the detected THz signals since only the y component of the emitted THz wave is detected. Since the field of 2.1 kOe is well above the saturation field, we can conclude that the peak signals at $\theta = 90°$ and 270° in Fig. 3(a) should not be ascribed to the unsaturation effect.

One may argue if the observed anisotropy is associated with polarization of the pump laser or θ-dependent light absorption. We observe a similar curve shape with the peak signals always at $\theta = 90°$ and 270° while rotating the polarization of the pump laser by 90°. The θ dependence of light absorption clearly deviates from the anisotropic θ-dependent THz emission, as seen in Figs. 3(b) and 3(c). This result indicates that our observation cannot be attributed to the change in the laser polarization direction with respect to a fixed crystal axis. In addition, Fig. 3(d) demonstrates that the THz emission associated with the crystal symmetry is independent of the laser intensity, i.e., the measured THz signals at $\theta = 90°$ and 270° are always larger than those at other angles under different laser fluences. Evidently, the anisotropic THz emission in the Fe/Pt(110) bilayer cannot originate from pure optical effects in the experiments.

At this stage, we can expect that some intrinsic mechanism(s) due to crystal anisotropy should play a key role. Based on the previous description of the STE [see Fig. 2(a)], the related anisotropy can occur in the following processes [4]: (1) spin-current generation in the Fe layer, (2) spin-current transmission through the Fe/Pt interface, (3) SCC in the Pt layer, and (4) THz wave emission induced by the transient charge current. Since the second and third processes are extremely difficult to directly access in the experiments, we might initially focus on discussing the first and last processes.

The spin-current generation process is generally associated with ultrafast demagnetization in Fe films via angular moment loss due to photoexcitation [44,45]. Photoinduced demagnetization might depend on the initial magnetization via the density of states in the material [24]. One may thus suspect whether the ultrafast demagnetization arising from the θ-dependent magnetization will lead to anisotropic spin-current generation. Therefore, we perform TR-MOKE measurements on the Fe(2 nm)/Pt(2 nm)/MgO(110) sample. Figure 4 shows the measured ultrafast demagnetization curves under a field of 2.5 kOe along Pt[001] and [$1\bar{1}0$]. Both demagnetization curves exhibit a similar quick quench of the magnetization at the subpicosecond timescale, followed by a slow recovery within several hundred picoseconds. For H||Pt[$1\bar{1}0$], the recovery process contains an obvious oscillation, while for H||Pt[001] the relaxation process has no oscillatory feature. The oscillation signal should be attributed to the laser-induced variation in magnetocrystalline anisotropy [41,46]. When a magnetic field is applied along the hard axis, such anisotropic variation can generate a significant spin precession. However, in the case of a magnetic field along the easy axis, spin precession can hardly occur due to the collinear alignment between the applied field and the magnetocrystalline anisotropy field [47]. It is worthwhile to note that, both curves in Fig. 4 show the same demagnetization ratio $\Delta M/M_0$, where ΔM and M_0 denote the magnitude of demagnetization and the saturated magnetization, respectively. Since the demagnetization signal does not depend on the magnetization orientation, it is reasonable to conclude that the spin-current generation process has no anisotropic behavior.

As noted by Seifert *et al.* [5], the THz wave emission is strongly related to the sheet conductance and is inversely proportional to the effective refractive index $n_{\mathrm{MgO}} + n_{\mathrm{air}} + z_0\tilde{G}$. Here, $n_{\mathrm{MgO}} = 2.98$ and $n_{\mathrm{air}} = 1$ are the refractive indices of MgO and air [8,12], respectively, $\tilde{G}$ is the total conductance of the bilayer at the THz frequency, and $z_0 \approx 377\Omega$ is the vacuum impedance. Therefore, a natural postulation is that anisotropic conductance may result in anisotropic THz emission. To check this presumption, we perform orientation-dependent transport measurements on a Pt(2 nm)/MgO(110) sample. As shown by the optical image in Fig. 5(a), Hall bars with different orientations are prepared on the same single-crystal film with identical growth conditions. This allows us to study anisotropic resistance by continuously rotating the current orientation in the single crystal [24]. Figure 5(b) illustrates the

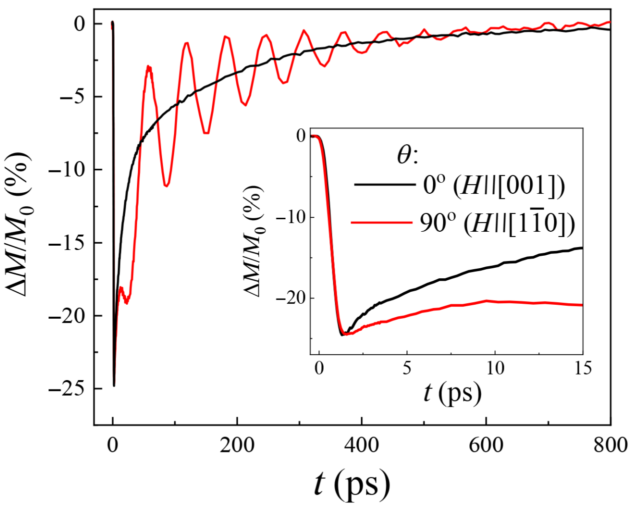

FIG. 4. Time-resolved magneto-optical Kerr signals from a Fe(2 nm)/Pt(2 nm)/MgO(110) sample. A magnetic field of 2500 Oe is applied along Pt[001] (black curve) or Pt [$1\bar{1}0$] (red curve). The inset emphasizes the photon-induced ultrafast demagnetization signals within a timescale of 15 ps, and the signal deviation for $t > 1.5$ ps is due to the photon-induced magnetization oscillation.

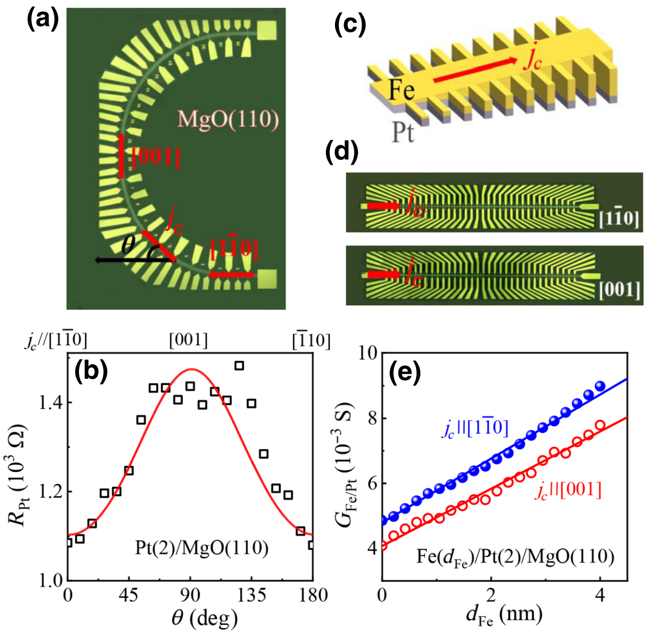

FIG. 5. (a) The device for the orientation-dependent transport measurements on the Pt(2 nm)/MgO(110) sample. (b) The orientation-dependent resistance measured from the device in (a). (c) Schematic of the thickness-dependent electrical transport measurements on the Fe/Pt bilayer with the Fe layer grown into a wedge shape. (d) Images of two Fe wedged devices with the current flowing along Pt [1$\bar{1}$0] and Pt[001]. (e) $d_{\rm Fe}$-dependent conductance of the Fe($d_{\rm Fe}$)/Pt(2 nm)/MgO(110) samples measured from two devices in (d).

measured resistance of the Pt film grown on MgO(110), which clearly shows the minimum and maximum values for the current j_c along Pt [1$\bar{1}$0] and Pt[001], respectively. The smaller conductance for j_c||Pt[001] then leads to the larger THz emission along Pt[001], which is in agreement with our THz measurement, where a larger THz emission for H||Pt [1$\bar{1}$0] is observed considering $\mathbf{j}_c$ is always perpendicular to **M**.

We also conduct similar transport experiments on the Fe($d_{\rm Fe}$)/Pt(2 nm)/MgO(110) samples. The Fe film is grown into a wedge shape, which can make the thickness of the Fe layer vary continuously in a single sample [26,48]. The Hall bars are prepared for the current flowing along the wedge direction, as shown in Fig. 5(c). We prepare two samples [see Fig. 5(d)] for experiments with the current along Pt [1$\bar{1}$0] and Pt[001]. To ensure that both samples had the same preparation conditions, they are grown at the same time. Figure 5(e) shows the $d_{\rm Fe}$-dependent conductance for the two current orientations. Clearly, both conductance values increase linearly with $d_{\rm Fe}$. However, the one measured for j_c||Pt [1$\bar{1}$0] is always larger than that for j_c||Pt[001]. Since the total conductance G should be equal to $\sigma_{\rm pt}d_{\rm pt} + \sigma_{\rm Fe}d_{\rm Fe}$, $\sigma_{\rm pt}$ and $\sigma_{\rm Fe}$ can be extracted from the data in Fig. 5(e). The derived $\sigma_{\rm pt}$ values are thus $(2.04 \pm 0.02)\times10^6$ S/m for j_c||Pt[001] and $(2.40 \pm 0.02)\times10^6$ S/m for j_c||Pt [1$\bar{1}$0]. Accordingly, an approximately 17.7% conductivity difference between these two orientations exists. The $\sigma_{\rm Fe}$ values for the current along Pt[001] and [1$\bar{1}$0] are estimated to be $(0.88 \pm 0.01)\times10^6$ S/m and $(0.98 \pm 0.04)\times10^6$ S/m, respectively. Specifically, the corresponding conductance for j_c||Pt [1$\bar{1}$0] in the Fe(2 nm)/Pt(2 nm) bilayer is approximately 15.7% larger than that for j_c||Pt[001]. Because the conductivity of the Pt layer is nearly twice that of the Fe layer, the orientation-dependent conductance in the Fe/Pt bilayer should be dominated by the anisotropic conductivity in the Pt layer. Indeed, the measured anisotropic conductance in the Fe/Pt(110) bilayer is consistent with the reported result in the Co/Pt(110) bilayer grown on MgO(110), where a larger resistivity occurs for j_c||Pt[001] [49].

Based on the anisotropic dc conductance in the Fe/Pt bilayer, we can evaluate its contribution to the anisotropic THz emission. Note that because the conductance in an ultrathin film is approximately frequency independent due to the high Drude scattering rate [18,50], $\tilde{G}$ can be regarded as G measured in the dc experiments. With the condition of $\mathbf{M}\perp\mathbf{j}_c$, the anisotropic ratio of THz emission due to crystal orientation-dependent conductance can be calculated by

$$\frac{\Delta V(H||[1\bar{1}0]) - \Delta V(H||[001])}{\Delta V(H||[001])} = \frac{\tilde{G}(j_c||[1\bar{1}0]) + (n_{\rm MgO} + n_{\rm air})/z_0}{\tilde{G}(j_c||[001]) + (n_{\rm MgO} + n_{\rm air})/z_0} - 1. \tag{1}$$

Using Eq. (1) we can estimate the anisotropy ratio of the THz emission to be approximately 5.6%. Although this value is much smaller than the experimental value of approximately 11.0%, the above analysis nonetheless demonstrates that the anisotropic conductance can at least partially explain the observed anisotropic THz emission.

As mentioned earlier, it is very hard to experimentally identify whether the spin-current transmission at the Fe/Pt interface and the SCC in the Pt layer also display anisotropic behavior. Therefore, in the next section we report an investigation on these two issues utilizing the method of first-principles calculation combined with superdiffusive spin-transport simulations. In addition, the orientation-dependent transport properties in Pt film are theoretically determined to confirm the consistency between the experimental and theoretical calculations.

IV. THEORETICAL CALCULATION

We first calculate the spin- and energy-dependent electron transmittance related to interface scattering, utilizing a well-developed transport theory based on the Landauer-Büttiker formalism combined with the self-consistent electronic structure of real materials [29,51]. In calculating the Fe(211)/Pt(110) interface, the in-plane lattice constants of the Pt layer are set according to the experimental values, which are stretched along Pt[001] and compressed along Pt $[1\bar{1}0]$ by factors of approximately 2.5% and -1.5% compared to their bulk lattice constants, respectively. The in-plane lattice of the Fe(211) layer is set to match the lattice of the Pt(110) surface. The atomic layer spacings along the out-of-plane direction for both the Fe and Pt layers are calculated by keeping the atomic volumes conserved. Within the framework of density-functional theory, the electronic structure of the interface is self-consistently determined by the atomic sphere approximation using the surface Green's function method implemented with a tight-binding linear muffin-tin orbital basis [52]. A minimal basis consisting of *s*, *p*, and *d* orbitals is used, and the two-dimensional (2D) Brillouin zone is sampled by a $k_{||}$ mesh with a constant density corresponding to 100×100 for a Pt primitive unit cell.

Figures 6(a)–6(d) show the calculated energy-dependent electron transmittances through the Fe(211)/Pt(110) interface. To clarify whether the spin-current transmission through the Fe/Pt interface depends on the **M** orientation, the transmittances for both spin-up and spin-down electrons are calculated with **M** fixed along either the Pt $[1\bar{1}0]$ or Pt[001] directions. As a general trend, the transmittance of spin-up electrons is larger than that of spin-down electrons for both transport directions, leading to a spin-filtering effect [53]. Such a spin-filtering effect is also observed at the bcc-Fe(001)/fcc-Pt(001) interface [54]. Figures 6(a) and 6(c) show the transmittances for the electrons moving across the interface from the Fe layer to the Pt layer (Fe→Pt), where the electron transmittances are nearly identical for both **M** orientations. For electron transport from Pt to Fe (Pt→Fe), the calculated transmittances also indicate little dependence on the magnetization orientation, as shown in Figs. 6(b) and 6(d).

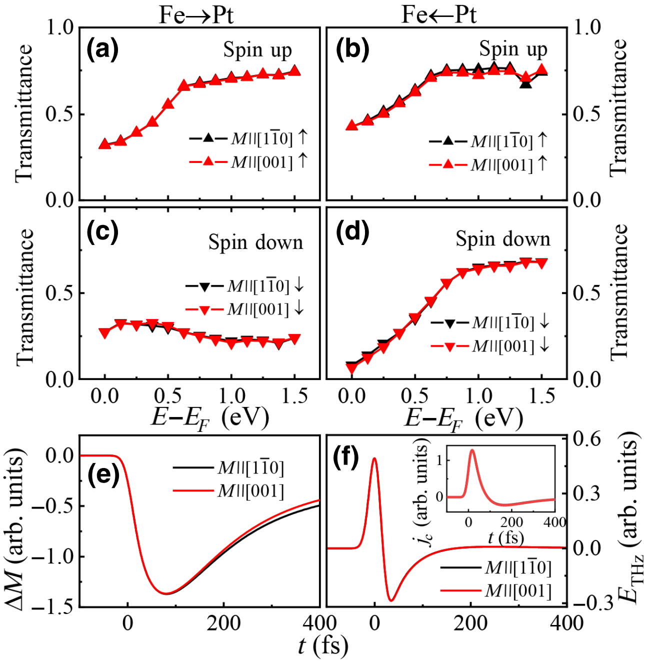

FIG. 6. (a)–(d) Spin-dependent electronic transmittance of the Fe(211)/Pt(110) interface as a function of energy. The Fe magnetization was aligned along either Pt $[1\bar{1}0]$(black symbols) or Pt[001] (red symbols). (a),(c) Calculated transmittances for the electron moving from Fe to Pt (Fe→Pt). (b),(d) Calculated transmittance for the electron from Pt to Fe (Pt→Fe). (e) The calculated photon-induced demagnetization curves with **M**||Pt $[1\bar{1}0]$ or **M**||Pt[001]. (f) The calculated time-domain THz signals and charge-current pulses from the Fe(2 nm)/Pt(5 nm) system with two magnetization orientations.

With realistic values of the interface transmittance, the photoinduced ultrafast magnetization dynamics can be further calculated using the superdiffusive spin-transport model [43,54]. In the calculation, the excitation laser pulse is set as a Gaussian function with a wavelength of 780 nm (approximately 1.5 eV) and a full width at half maximum of 30 fs. Figure 6(e) shows the calculated ultrafast demagnetization of Fe in the Fe(2 nm)/Pt(5 nm) bilayer with Fe magnetization **M** along either Pt$[1\bar{1}0]$ or Pt[001], where only an approximately 0.34% difference in the demagnetization can be observed. It should be noted that in addition to the superdiffusive spin transport through the Fe/Pt interface, there are other mechanisms that dissipate the spin angular momentum [55–57], which can contribute to the total ultrafast demagnetization shown in Fig. 4. Nevertheless, our experimental measurements and theoretical calculations indicate that no mechanisms could induce a noticeable **M**-orientation dependence of ultrafast demagnetization in the Fe(211)/Pt(110) system. We further calculate the THz emission by the spin current injected through the Fe/Pt interface by only taking the **M**-orientation-dependent interface transmittance into account. Then, as shown in Fig. 6(f), there is only a -0.17% difference in the THz intensity between **M**||Pt $[1\bar{1}0]$ and **M**||Pt[001]. In our calculation, only electrons in Fe excited by the laser are considered. Including the laser absorption in Pt would slightly increase the loss of spin-up hot electrons in Pt due to the spin filtering at the Fe/Pt interface and thus decreases the total THz amplitude, which is however still **M** orientation independent. Therefore, the results confirm that the observed anisotropic THz emission cannot be attributed to spin-dependent electron transmission through the Fe/Pt interface.

The experimental measurements in Fig. 5 already show that the conductivity of the Fe(211)/Pt(110) bilayer has a significant crystal-orientation dependence, which mainly results from the contribution of the Pt layer. Theoretical calculation of the resistivity requires prior knowledge of the specific types of microscopic disorders, which is impossible to determine either experimentally or theoretically. Therefore, we investigate the Sharvin conductance G_{Sh} of the Pt layer, which is more generic for characterizing the transport properties of a particular metal because it describes the number of transverse channels per spin and the unit area of normal metal, or equivalently the number of Fermi surface sheets projected along the transport direction [58,59]. Within the Landauer-Büttiker formalism, $G^{\sigma}_{\mathrm{Sh}}(E)$ can be calculated by the total number of propagating states $N^{\sigma}(\mathbf{k}_{||}, E)$,

$$G^{\sigma}_{\mathrm{Sh}}(E) = \frac{e^2}{hAN_{k_{||}}} \sum_{k_{||}} N^{\sigma}(k_{||}, E) \tag{2}$$

where e^2/h is the quantized electronic conductance for a single spin channel, $N_{k_{||}}$ is the total number of $\mathbf{k}_{||}$ in the 2D Brillouin zone perpendicular to the current direction, σ is the spin channel, and A is the cross-sectional area of the lateral supercell in the calculation. Note that nonmagnetic Pt has the same energy-dependent Sharvin conductance for both spin channels, i.e., $G^{\uparrow}{}_{\mathrm{Sh,Pt}}(E) = G^{\downarrow}{}_{\mathrm{Sh,Pt}}(E) = G_{\mathrm{Sh}}$.

We first calculate the G_{Sh} of fcc Pt without structural distortion. Figure 7(a) shows the calculated G_{Sh} within the electron energy range of 0–1.5 eV for electron transport along Pt$[1\bar{1}0]$ and [001]. At the Fermi energy (E_F), the calculated G_{Sh} is $0.67 \times 10^{15}\ \Omega^{-1}\,\mathrm{m}^{-2}$ for $j_c||[001]$ and $0.71 \times 10^{15}\ \Omega^{-1}\,\mathrm{m}^{-2}$ for $j_c||[1\bar{1}0]$. Despite its complex Fermi surface, the propagating channels are nearly isotropic for Pt. With an increasing electronic energy, G_{Sh} first decreases and reaches a minimum at approximately 0.6 eV, corresponding to the top 5d bands, and then increases slightly at a higher energy. However, if the distorted Pt structure with the experimental values is used, the calculated G_{Sh} shows a significant difference for energies below 0.6 eV, as shown in Fig. 7(b). This indicates that the 5d bands exhibit a larger sensitivity to lattice distortion than the free-electron-like 6s band. G_{Sh} at E_F in the distorted Pt layer is $0.74\times10^{15}\ \Omega^{-1}\,\mathrm{m}^{-2}$ for $j_c||[1\bar{1}0]$, which is larger than that calculated in the undistorted Pt structure. On the other hand, G_{Sh} at E_F for $j_c||[001]$ is almost the same for both cases with distorted and undistorted Pt lattices.

We further plot the distribution of the conductance channels at E_F in the 2D Brillouin zone to understand the effect of lattice distortion. Figures 7(c) and 7(d) show the calculated conductance channels of Pt in the [001] direction for the undistorted and distorted structures, respectively. These very similar images imply that the transport properties along [001] are relatively insensitive to structural distortion, which is in agreement with the same G_{Sh} calculated for both cases. In the Pt$[1\bar{1}0]$ direction, the distribution of conductance channels shows remarkable variation due to the distortion, as shown in Figs. 7(e) and 7(f). The calculated number of channels for the distorted structure increases in the large area in the 2D Brillouin zone, as marked by the red dashed circles in Fig. 7(f) compared with the distribution in Fig. 7(e) for the undistorted structure. These changes in the conductance channels essentially lead to a noticeable increase in the calculated G_{Sh} of the distorted Pt for $j_c||[1\bar{1}0]$. This increase is consistent with the experimental measurements in Fig. 5. Based on the calculated $G_{\mathrm{Sh}}(E)$, we can further estimate the electron field profile of the THz emission [54]. For the undistorted Pt structure, the calculated THz

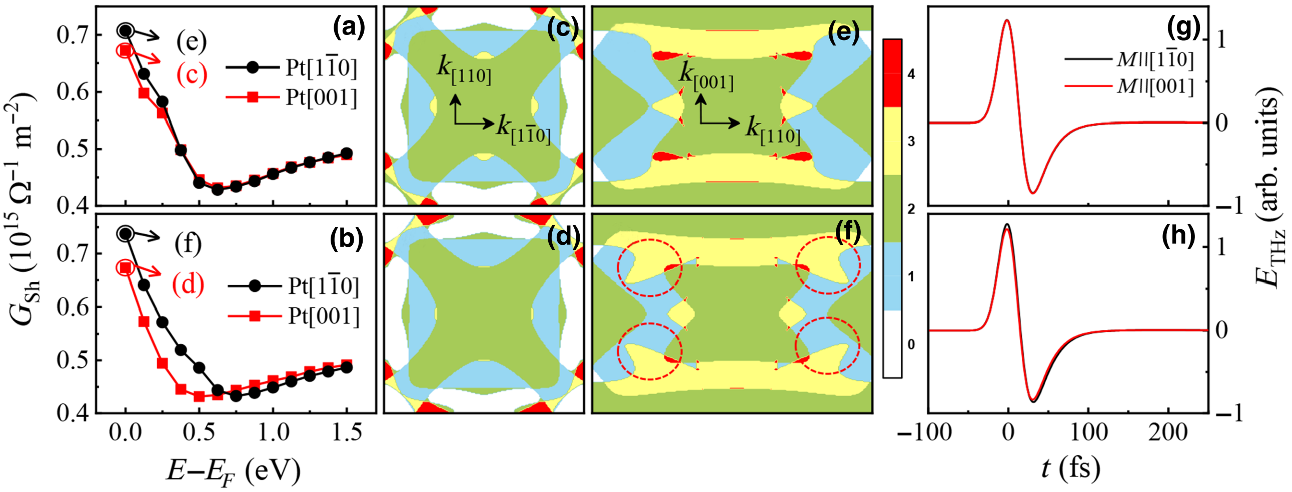

FIG. 7. Calculated Sharvin conductance G_{sh} of Pt as a function of energy with (a) the fcc structure and (b) the distorted structure determined by the experiment. The current flows along either the Pt$[1\bar{1}0]$ (black line) or Pt [001] (red line) directions. (c)−(f) Distribution of the conduction channels in the 2D Brillouin zone at E_F for the current along Pt[001] [(c),(d)] and Pt$[1\bar{1}0]$ [(e),(f)]. (g), (h) Calculated time-domain THz signals for **M**||Pt$[1\bar{1}0]$ or **M**||Pt[001]. (a), (c), (e), and (g) are calculated using the cubic structure of Pt with its bulk lattice constant, while (b), (d), (f), and (h) are calculated using the distorted Pt lattice structure determined experimentally.

spectrum in Fig. 7(g) only shows an approximately -0.02% difference for **M**||Pt$[1\bar{1}0]$ relative to **M**||Pt[001]. However, for the distorted Pt structure, the anisotropic conductance can induce an approximately 4.4% difference in the calculated THz spectra for **M**||Pt$[1\bar{1}0]$ relative to **M**||Pt[001], as shown in Fig. 7(h). The calculated THz anisotropy due to the anisotropic conductance agrees well with the experimental conductance anisotropy of approximately 4.9% in Fig. 5 but is still less than the experimental anisotropy value of approximately 11.0% in the measured total THz signal.

It is well known that a larger ISHE in heavy metals can generate stronger THz emissions [7,11]. Freimuth *et al.* reported that the SCC efficiency of transition metals with hcp structures strongly depends on their magnetization orientation [22]. The anisotropic ISHE is another possible mechanism for the anisotropic THZ emission. To quantitatively examine the ISHE, we consider a spin current injected into Pt along the [110] axis with its polarization along either Pt[001] or Pt$[1\bar{1}0]$. Using the above configurations, we calculate the corresponding spin Hall conductivity (SHC). Figure 8(a) shows the calculated SHC of undistorted Pt as a function of energy, which is nearly identical for the two spin polarization configurations, i.e., it decreases monotonically with an increasing energy. This confirms that the SHCs with two perpendicular spin orientations are equal in a cubic metal by symmetry analysis [22,60]. Then we calculate the SHC in the system with the distorted Pt lattice. As shown in Fig. 8(b), σ_{SH} has a significant difference between the two spin orientations. In the inset we plot the relative SHC ratio defined as

$$\frac{\Delta\sigma}{\sigma} = \frac{\sigma_{[1\bar{1}0]} - \sigma_{[001]}}{\sigma_{[001]}},$$

which is approximately 10% at E_F. This decreases to a negative value for energies above 0.5 eV and implies a significant anisotropy in the SCC efficiency, depending on the polarization orientation of the injected spin current. Therefore, the calculations demonstrate that the anisotropy of SHC is induced by lattice distortion in the Pt(110) film, which breaks the in-plane lattice symmetry. It is worth noting that the anisotropic spin Hall effect has been reported on experimentally in $\mathrm{WTe_2}$ with the broken symmetry of the in-plane lattice [61,62].

Our studies demonstrated that the anisotropic THz emission in the Fe/Pt/MgO(110) system is induced by both electronic conductivity and SHC due to the distorted lattice structure. Then we further apply the superdiffusive spin-transport model and computed the fs-laser-induced THz emission by simultaneously including these two factors [5,29]. The calculated time-domain THz spectra of the Fe(211)/Pt(110) bilayer in Fig. 9 show that the THz emission with Fe magnetization along Pt$[1\bar{1}0]$ is 11.3% larger than that with **M**||Pt[001], which is in excellent agreement with the experimental value of 11.0% in Fig. 2.

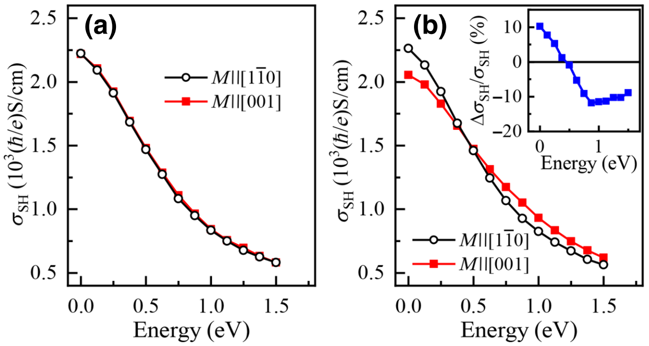

FIG. 8. Calculated SHC of Pt as a function of energy with (a) the fcc structure and (b) the distorted structure determined experimentally. The spin current always flows along the [110] direction. The black and red symbols correspond to the polarization of the spin current along $[1\bar{1}0]$ and [001], respectively. The inset in (b) shows the relative SHC ratio as a function of energy.

Note that the anisotropy of both the conductance and SHC in Figs. 7 and 8 are induced by the in-plane lattice distortion. Therefore, our studies not only reveal the possibility of modifying the THz emission in FM-HM bilayers utilizing the **M** orientation, but also suggest one possible route of manipulating the SHC by applying the in-plane strain. The film strain can influence the SOC effect and its other related spintronic properties, e.g., anisotropic magnetoresistance, anomalous Hall effect, and spin-orbit torque.

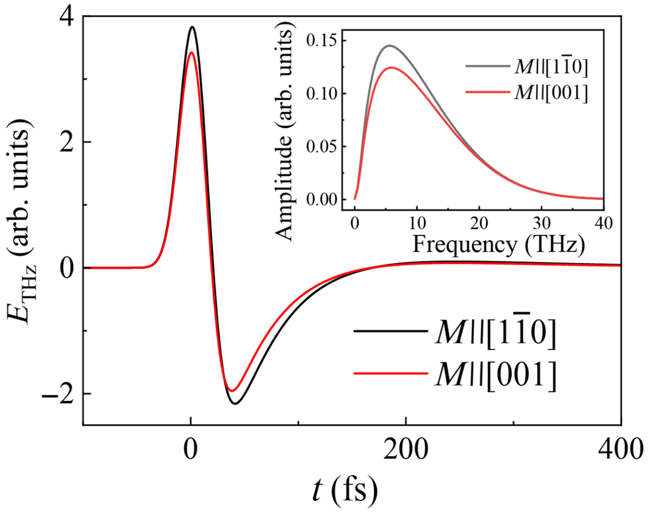

FIG. 9. Laser-induced time-domain THz signals in a Fe(211)/Pt(110) system with a distorted lattice structure by including the anisotropic conductance and the SHC. The red and black curves are the calculated results with **M**||Pt$[1\bar{1}0]$ and **M**||Pt[001], respectively. There is an 11.3% deference of the two THz spectra. The inset shows the corresponding Fourier transformed spectra of the THz signals in the frequency domain.

Such phenomena deserve future experimental and theoretical exploration. Recent investigations demonstrate that the THz time-domain spectroscopy (THz TDS) can be used as a fine probe of the metallic conductivity to investigate the anisotropic magnetoresistance in magnetic thin films and giant magnetoresistance in magnetic multilayers up to THz frequency range [50,63], then the anisotropic conductance measured in a Fe(211)/Co(110) system can be further investigated with the THz TDS.

V. CONCLUSIONS

In summary, we demonstrate that the fs-laser-induced THz emission from single-crystal Fe(211)/Pt(110) bilayers strongly depends on the magnetization orientation. This provides us with a possible way to tune the THz emission in a homogeneous FM-NM bilayer. Our studies show that both the spin-current generation and subsequent transport into the attached Pt layer are independent of the magnetization orientation, and have no contribution to the observed anisotropic THz emission. However, the SCC in the Pt layer and THz radiation can be strongly related to the **M** orientation due to the anisotropic SHC and longitudinal conductance in the Fe/Pt bilayer, which eventually give rise to the anisotropic THz emission. Based on the contribution of anisotropic SHC and longitudinal conductance, the calculated THz emission in Fe(211)/Pt(110) system with **M**||Pt[$1\bar{1}0$] is 11.3% larger than that with **M**||Pt[001], in excellent agreement with the experimental anisotropic ratio of 11.0%. The first-principles calculation also reveals that the anisotropy of both SHC and conductance are induced by the distorted lattice in the Pt(110) film, due to the epitaxial strain for the Fe/Pt bilayer grown on MgO(110). Our studies indicate a promising way to utilize strain in modifying the physical properties related to the SOC effect in spintronic devices.

ACKNOWLEDGMENTS

This work at Fudan University is supported by the National Natural Science Foundation of China (NSFC, Grants No. 11734006, No. 11974079, and No. 11774064), the National Key Research and Development Program of China (Grant No. 2016YFA0300703), and the Shanghai Municipal Science and Technology Major Project (Grant No. 2019SHZDZX01). The work at Beijing Normal University is supported by NSFC (Grants No. 61774018 and No. 11734004). The work at the University of Electronic Science and Technology of China is supported by NSFC (Grant No. 11974070) and the Chinese Academy of Sciences Interdisciplinary Innovation Team.

[1] M. Tonouchi, Cutting-edge terahertz technology, Nat. Photonics **1**, 97 (2007).

[2] B. Ferguson and X.-C. Zhang, Materials for terahertz science and technology, Nat. Mater. **1**, 26 (2002).

[3] P. U. Jepsen, D. G. Cooke, and M. Koch, Terahertz spectroscopy and imaging – modern techniques and applications, Laser. Photon. Rev. **5**, 124 (2011).

[4] T. Kampfrath, M. Battiato, P. Maldonado, G. Eilers, J. Nötzold, S. Mährlein, V. Zbarsky, F. Freimuth, Y. Mokrousov, S. Blügel, M. Wolf, I. Radu, P. M. Oppeneer, and M. Münzenberg, Terahertz spin current pulses controlled by magnetic heterostructures, Nat. Nanotechnol. **8**, 256 (2013).

[5] T. Seifert, et al., Efficient metallic spintronic emitters of ultrabroadband terahertz radiation, Nat. Photonics **10**, 483 (2016).

[6] D. Yang, J. Liang, C. Zhou, L. Sun, R. Zheng, S. Luo, Y. Wu, and J. Qi, Powerful and tunable THz emitters based on the Fe/Pt magnetic heterostructure, Adv. Opt. Mater. **4**, 1944 (2016).

[7] Y. Wu, M. Elyasi, X. Qiu, M. Chen, Y. Liu, L. Ke, and H. Yang, High-Performance THz emitters based on ferromagnetic/nonmagnetic heterostructures, Adv. Mater. **29**, 1603031 (2017).

[8] G. Torosyan, S. Keller, L. Scheuer, R. Beigang, and E. T. Papaioannou, Optimized spintronic terahertz emitters based on epitaxial grown Fe/Pt layer structures, Sci. Rep. **8**, 1311 (2018).

[9] T. Seifert, S. Jaiswal, M. Sajadi, G. Jakob, S. Winnerl, M. Wolf, M. Kläui, and T. Kampfrath, Ultrabroadband single-cycle terahertz pulses with peak fields of 300 kV cm^{-1} from a metallic spintronic emitter, Appl. Phys. Lett. **110**, 252402 (2017).

[10] Z. Feng, R. Yu, Y. Zhou, H. Lu, W. Tan, H. Deng, Q. C. Liu, Z. H. Zhai, L. G. Zhu, J. W. Cai, B. F. Miao, and H. F. Ding, Highly efficient spintronic terahertz emitter enabled by metal-dielectric photonic crystal, Adv. Opt. Mater. **6**, 1800965 (2018).

[11] T. J. Huisman, R. V. Mikhaylovskiy, J. D. Costa, F. Freimuth, E. Paz, J. Ventura, P. P. Freitas, S. Blugel, Y. Mokrousov, T. Rasing, and A. V. Kimel, Femtosecond control of electric currents in metallic ferromagnetic heterostructures, Nat. Nanotechnol. **11**, 455 (2016).

[12] C. Zhou, Y. P. Liu, Z. Wang, S. J. Ma, M. W. Jia, R. Q. Wu, L. Zhou, W. Zhang, M. K. Liu, Y. Z. Wu, and J. Qi, Broadband Terahertz Generation via the Interface Inverse Rashba-Edelstein Effect, Phys. Rev. Lett. **121**, 086801 (2018).

[13] J. C. R. Sánchez, L. Vila, G. Desfonds, S. Gambarelli, J. P. Attané, J. M. De Teresa, C. Magén, and A. Fert, Spin-to-charge conversion using Rashba coupling at the interface between non-magnetic materials, Nat. Commun. **4**, 2944 (2013).

[14] M. B. Jungfleisch, Q. Zhang, W. Zhang, J. E. Pearson, R. D. Schaller, H. Wen, and A. Hoffmann, Control of Terahertz Emission by Ultrafast Spin-Charge Current Conversion at Rashba Interfaces, Phys. Rev. Lett. **120**, 207207 (2018).

[15] J. Li, Z. Jin, B. Song, S. Zhang, C. Guo, C. Wan, X. Han, Z. Cheng, C. Zhang, X. Lin, G. Ma, and J. Yao, Magnetic-field-free terahertz emission from a magnetic tunneling junction, Jpn. J. Appl. Phys. **58**, 090913 (2019).

[16] Z. Jin, S. Zhang, W. Zhu, Q. Li, W. Zhang, Z. Zhang, S. Lou, Y. Dai, X. Lin, and G. Ma, Terahertz radiation

modulated by confinement of picosecond current based on patterned ferromagnetic heterostructures, Physica Status Solidi (RRL)–Rapid Res. Lett. **13**, 1900057 (2019).

[17] B. Song, Y. Song, S. Zhang, K. Jin, W. Zhu, Q. Li, Z. Zhang, X. Lin, Y. Dai, and X. Yan, Controlling terahertz radiation with subwavelength blocky patterned CoFeB/Pt heterostructures, Appl. Phys. Express **12**, 122003 (2019).

[18] T. S. Seifert, N. M. Tran, O. Gueckstock, S. M. Rouzegar, L. Nadvornik, S. Jaiswal, G. Jakob, V. V. Temnov, M. Münzenberg, M. Wolf, M. Kläui, and T. Kampfrath, Terahertz spectroscopy for all-optical spintronic characterization of the spin-hall-effect metals Pt, W and Cu80Ir20, J. Phys. D: Appl. Phys. **51**, 364003 (2018).

[19] M. Chen, R. Mishra, Y. Wu, K. Lee, and H. Yang, Terahertz emission from compensated magnetic heterostructures, Adv. Opt. Mater. **6**, 1800430 (2018).

[20] M. J. Chen, Y. Wu, Y. Liu, K. Lee, X. P. Qiu, P. He, J. W. Yu, and H. Yang, Current-Enhanced broadband THz emission from spintronic devices, Adv. Opt. Mater. **7**, 1801608 (2019).

[21] D. Y. Kong, X. J. Wu, B. Wang, T. X. Nie, M. Xiao, C. Pandey, Y. Gao, L. G. Wen, W. S. Zhao, C. J. Ruan, J. G. Miao, Y. T. Li, and L. Wang, Broadband spintronic terahertz emitter with magnetic-field manipulated polarizations, Adv. Opt. Mater. **7**, 1900487 (2019).

[22] F. Freimuth, S. Blügel, and Y. Mokrousov, Anisotropic Spin Hall Effect from First Principles, Phys. Rev. Lett. **105**, 246602 (2010).

[23] W. Zhang, M. B. Jungfleisch, F. Freimuth, W. Jiang, J. Sklenar, J. E. Pearson, J. B. Ketterson, Y. Mokrousov, and A. Hoffmann, All-electrical manipulation of magnetization dynamics in a ferromagnet by antiferromagnets with anisotropic spin hall effects, Phys. Rev. B **92**, 144405 (2015).

[24] F. L. Zeng, Z. Y. Ren, Y. Li, J. Y. Zeng, M. W. Jia, J. Miao, A. Hoffmann, W. Zhang, Y. Z. Wu, and Z. Yuan, Intrinsic Mechanism for Anisotropic Magnetoresistance and Experimental Confirmation in $\mathrm{Co}_x\mathrm{Fe}_{1-x}$ Single-Crystal Films, Phys. Rev. Lett. **125**, 097201 (2020).

[25] Y. Li, F. Zeng, S. S. L. Zhang, H. Shin, H. Saglam, V. Karakas, O. Ozatay, J. E. Pearson, O. G. Heinonen, Y. Wu, A. Hoffmann, and W. Zhang, Giant Anisotropy of Gilbert Damping in Epitaxial CoFe Films, Phys. Rev. Lett. **122**, 117203 (2019).

[26] J. X. Li, M. W. Jia, Z. Ding, J. H. Liang, Y. M. Luo, and Y. Z. Wu, Pt-enhanced anisotropic magnetoresistance in Pt/Fe bilayers, Phys. Rev. B **90**, 214415 (2014).

[27] K. Serizawa, M. Ohtake, T. Kawai, M. Futamoto, F. Kirino, and N. Inaba, Influence of crystal orientation on the magnetostriction behavior of Fe films formed on MgO single-crystal substrates, J. Magn. Magn. Mater. **477**, 420 (2019).

[28] J. L. Vassent, A. Marty, and B. Gilles, Indium superstructures on the Fe (211) surface, Appl. Surf. Sci. **78**, 357 (1994).

[29] See Supplemental Material at http://link.aps.org/supplemental/10.1103/PhysRevApplied.15.044022 for details on crystalline structure analysis, magnetic property measurements, calculation methods, and some other problems involved in the text, which includes Refs. [30–38].

[30] R. L. Stamps, L. Louail, M. Hehn, M. Gester, and K. Ounadjela, Anisotropies, cone states, and stripe domains in Co/Pt multilayers, J. Appl. Phys. **81**, 4751 (1997).

[31] L. Sun, J. H. Liang, X. Xiao, C. Zhou, G. Chen, Y. Huo, and Y. Z. Wu, Magnetic stripe domains of [Pt/Co/Cu]10 multilayer near spin reorientation transition, AIP Adv. **6**, 056109 (2016).

[32] S. Datta, *Electronic Transport in Mesoscopic Systems* (Cambridge university press, Cambridge, 1995).

[33] M. A. M. Gijs and G. E. W. Bauer, Perpendicular giant magnetoresistance of magnetic multilayers, Adv. Phys. **46**, 285 (1997).

[34] J. Qiao, J. Zhou, Z. Yuan, and W. Zhao, Calculation of intrinsic spin Hall conductivity by Wannier interpolation, Phys. Rev. B **98**, 214402 (2018).

[35] Y. Yao and Z. Fang, Sign Changes of Intrinsic Spin Hall Effect in Semiconductors and Simple Metals: First-Principles Calculations, Phys. Rev. Lett. **95**, 156601 (2005).

[36] M. Gradhand, D. V. Fedorov, F. Pientka, P. Zahn, I. Mertig, and B. L. Györffy, First-principle calculations of the Berry curvature of Bloch states for charge and spin transport of electrons, J. Phys.: Condens. Matter **24**, 213202 (2012).

[37] L. Matthes, S. Küfner, J. Furthmüller, and F. Bechstedt, Intrinsic spin Hall conductivity in one-, two-, and three-dimensional trivial and topological systems, Phys. Rev. B **94**, 085410 (2016).

[38] P. Kužel, M. A. Khazan, and J. Kroupa, Spatiotemporal transformations of ultrashort terahertz pulses, J. Opt. Soc. Am. B **16**, 1795 (1999).

[39] G. Chen, J. Zhu, J. Li, F. Z. Liu, and Y. Z. Wu, Revealing the volume magnetic anisotropy of Fe films epitaxied on GaAs(001) surface, Appl. Phys. Lett. **98**, 132505 (2011).

[40] J. H. Liang, Y. L. Chen, L. Sun, C. Zhou, Y. Yang, and Y. Z. Wu, The anisotropic linear and quadratic magneto-optical Kerr effects in epitaxial Fe/GaAs(110) film, Appl. Phys. Lett. **108**, 082404 (2016).

[41] L. Q. Shen, L. F. Zhou, J. Y. Shi, M. Tang, Z. Zheng, D. Wu, S. M. Zhou, L. Y. Chen, and H. B. Zhao, Dominant role of inverse Cotton-Mouton effect in ultrafast stimulation of magnetization precession in undoped yttrium iron garnet films by 400-nm laser pulses, Phys. Rev. B **97**, 224430 (2018).

[42] Z. Zheng, J. Y. Shi, Q. Li, T. Gu, H. Xia, L. Q. Shen, F. Jin, H. C. Yuan, Y. Z. Wu, L. Y. Chen, and H. B. Zhao, Magneto-optical probe of ultrafast spin dynamics in antiferromagnetic CoO thin films, Phys. Rev. B **98**, 134409 (2018).

[43] M. Battiato, K. Carva, and P. M. Oppeneer, Superdiffusive Spin Transport as a Mechanism of Ultrafast Demagnetization, Phys. Rev. Lett. **105**, 027203 (2010).

[44] E. Beaurepaire, J. C. Merle, A. Daunois, and J. Y. Bigot, Ultrafast Spin Dynamics in Ferromagnetic Nickel, Phys. Rev. Lett. **76**, 4250 (1996).

[45] E. Turgut, C. La-o-vorakiat, J. M. Shaw, P. Grychtol, H. T. Nembach, D. Rudolf, R. Adam, M. Aeschlimann, C. M. Schneider, T. J. Silva, M. M. Murnane, H. C. Kapteyn, and S. Mathias, Controlling the Competition between Optically Induced Ultrafast Spin-Flip Scattering and Spin Transport in Magnetic Multilayers, Phys. Rev. Lett. **110**, 197201 (2013).

[46] K. Jhuria, J. Hohlfeld, A. Pattabi, E. Martin, A. Y. Arriola Córdova, X. Shi, R. Lo Conte, S. Petit-Watelot, J. C. Rojas-Sanchez, G. Malinowski, S. Mangin, A. Lemaître, M. Hehn, J. Bokor, R. B. Wilson, and J. Gorchon, Spin–orbit torque switching of a ferromagnet with picosecond electrical pulses, Nat. Electron. **3**, 680 (2020).

[47] T. P. Ma, S. F. Zhang, Y. Yang, Z. H. Chen, H. B. Zhao, and Y. Z. Wu, Distinguishing the laser-induced spin precession excitation mechanism in Fe/MgO(001) through field orientation dependent measurements, J. Appl. Phys. **117**, 013903 (2015).

[48] M. Jia, F. Zeng, X. Xiao, C. Zhou, X. Hu, and Y. Wu, Thickness-dependent angular dependent magnetoresistance in single-crystalline Co film and Co/Pt heterostructures, J. Magn. Magn. Mater. **508**, 166863 (2020).

[49] R. Thompson, J. Ryu, Y. Du, S. Karube, M. Kohda, and J. Nitta, Current direction dependent spin Hall magnetoresistance in epitaxial Pt/Co bilayers on MgO(110), Phys. Rev. B **101**, 214415 (2020).

[50] L. Nadvorník, M. Borchert, L. Brandt, R. Schlitz, K. A. de Mare, K. Výborný, I. Mertig, G. Jakob, M. Kläui, S. T. B. Goennenwein, M. Wolf, G. Woltersdorf, and T. Kampfrath, Broadband terahertz probes of anisotropic magnetoresistance disentangle extrinsic and intrinsic contributions. arXiv:2010.06280 (2020).

[51] K. Xia, P. J. Kelly, G. E. W. Bauer, I. Turek, J. Kudrnovský, and V. Drchal, Interface resistance of disordered magnetic multilayers, Phys. Rev. B **63**, 064407 (2001).

[52] I. Turek, V. Drchal, J. Kudrnovský, M. Sob, and P. Weinberger, *Electronic Structure of Disordered Alloys, Surfaces and Interfaces* (Kluwer, Boston, 1997).

[53] T. H. Dang, et al., Ultrafast spin-currents and charge conversion at 3d-5d interfaces probed by time-domain terahertz spectroscopy, Appl. Phys. Rev. **7**, 041409 (2020).

[54] W.-T. Lu, Y. Zhao, M. Battiato, Y. Wu, and Z. Yuan, Interface reflectivity of a superdiffusive spin current in ultrafast demagnetization and terahertz emission, Phys. Rev. B **101**, 014435 (2020).

[55] P. M. Oppeneer and A. Liebsch, Ultrafast demagnetization in Ni: Theory of magneto-optics for non-equilibrium electron distributions, J. Phys.: Condens. Matter **16**, 5519 (2004).

[56] B. Koopmans, M. van Kampen, J. T. Kohlhepp, and W. J. M. de Jonge, Ultrafast Magneto-Optics in Nickel: Magnetism or Optics?, Phys. Rev. Lett. **85**, 844 (2000).

[57] B. Vodungbo, et al., Indirect excitation of ultrafast demagnetization, Sci. Rep. **6**, 18970 (2016).

[58] M. Zwierzycki, Y. Tserkovnyak, P. J. Kelly, A. Brataas, and G. E. W. Bauer, First-principles study of magnetization relaxation enhancement and spin transfer in thin magnetic films, Phys. Rev. B **71**, 064420 (2005).

[59] Z. Yuan and P. J. Kelly, Spin-orbit-coupling induced torque in ballistic domain walls: Equivalence of charge-pumping and nonequilibrium magnetization formalisms, Phys. Rev. B **93**, 224415 (2016).

[60] E. M. Chudnovsky, Intrinsic spin hall effect in noncubic crystals, Phys. Rev. B **80**, 153105 (2009).

[61] J. Zhou, J. Qiao, A. Bournel, and W. Zhao, Intrinsic spin Hall conductivity of the semimetals $MoTe_2$ and WTe_2, Phys. Rev. B **99**, 060408 (2019).

[62] P. Seifert, F. Sigger, J. Kiemle, K. Watanabe, T. Taniguchi, C. Kastl, U. Wurstbauer, and A. Holleitner, In-plane anisotropy of the photon-helicity induced linear Hall effect in few-layer WTe_2, Phys. Rev. B **99**, 161403 (2019).

[63] Z. Jin, A. Tkach, F. Casper, V. Spetter, H. Grimm, A. Thomas, T. Kampfrath, M. Bonn, M. Kläui, and D. Turchinovich, Accessing the fundamentals of magnetotransport in metals with terahertz probes, Nat. Phys. **11**, 761 (2015).